ADVANCED MATERIALS
www.advmat.de

Tailoring Optical Properties in Transparent Highly Conducting Perovskites by Cationic Substitution

Mahdad Mohammadi, Ruiwen Xie, Niloofar Hadaeghi, Aldin Radetinac, Alexey Arzumanov, Philipp Komissinskiy, Hongbin Zhang, and Lambert Alff**

$SrMoO_3$, $SrNbO_3$, and $SrVO_3$ are remarkable highly conducting d^1 (V, Nb) or d^2 (Mo) perovskite metals with an intrinsically high transparency in the visible. A key scientific question is how the optical properties of these materials can be manipulated to make them suitable for applications as transparent electrodes and in plasmonics. Here, it is shown how 3d/4d cationic substitution in perovskites tailors the relevant materials parameters, i.e., optical transition energy and plasma frequency. With the example of the solid-state solution $SrV_{1-x}Mo_xO_3$, it is shown that the absorption and reflection edges can be shifted to the edges of the visible light spectrum, resulting in a material that has the potential to outperform indium tin oxide (ITO) due to its extremely low sheet resistance. An optimum for $x = 0.5$, where a resistivity of 32 µΩ cm (≈12 Ω sq^{-1}) is paired with a transmittance above 84% in the whole visible spectrum is found. Quantitative comparison between experiments and electronic structure calculations show that the shift of the plasma frequency is governed by the interplay of d-band filling and electronic correlations. This study advances the knowledge about the peculiar class of highly conducting perovskites toward sustainable transparent conductors and emergent plasmonics.

1. Introduction

Perovskite oxides have been intensively studied in the last decades due to their wealth of materials properties and the possibility to grow thin film heterostructures for various device applications. One of the less commonly discussed outstanding properties is the high metallic conductivity, e.g., in $SrMoO_3$ that even outperforms platinum at room temperature[1] and enables novel applications such as electrode material in oxide electronics.[2] Besides high conductivity,[3–5] three perovskite compounds $SrVO_3$ (SVO), $SrMoO_3$ (SMO), and $SrNbO_3$ (SNO) display an intrinsically high optical transparency,[6–10] making them ideal candidates as transparent conducting materials. The good metallic properties originate from the d^1 or d^2 electronic configuration of the B-site cation resulting in a large charge-carrier density, n_e, beyond 10^{22} cm^{-3}, being of the same order of magnitude as in conventional good metals. Moreover, as the B-site cations are all early transition-metal elements, the absence of the s–d scattering mechanism contributes to the high conductivity due to the energetic separation of the s- and d-states in these elements.[11] With respect to the optical properties, the most relevant physics is contained in the effective electron mass, m^*, enhancement in the narrow d-band[12–14] shifting the plasma frequency, ω_p, which is proportional to $\omega_p \approx \sqrt{n_e / m^*}$ from the ultraviolet (UV) for conventional metals into the visible or even infrared (IR) region. Therefore, the plasma frequency of transparent conducting perovskites has values between conventional metals (large ω_p) and highly doped semiconductors (low ω_p), in which the increase of the charge-carrier density by doping is limited. The origin of the effective mass enhancement has been recently discussed and can be, in the simplest case, described by a renormalization factor, Z_k, due to correlation effects.[12] However, electron–phonon coupling and low-dimensionality of the Fermi surfaces have to be taken into consideration to draw a more complete physical picture.[15] In addition to the suited plasma frequency, a sufficiently large optical transition energy E_g^{opt} and the absence of strong absorption features in the visible spectrum opens a transparency window and makes $SrVO_3$, $SrNbO_3$, and $SrMoO_3$ potential candidates for a range of optical and electronic applications such as water splitting photocatalysts,[16,17] transparent electrodes,[6,8,18] and low loss plasmonic materials.[19,20]

These various applications have different requirements on the transparent window energy range for optimal performance, therefore a handle to tailor the optical properties for different

M. Mohammadi, A. Radetinac, A. Arzumanov, P. Komissinskiy, L. Alff
Advanced Thin Film Technology Division
Institute of Materials Science
Technische Universität Darmstadt
Alarich-Weiss-Straße 2, 64287 Darmstadt, Germany
E-mail: lambert.alff@tu-darmstadt.de

R. Xie, N. Hadaeghi, H. Zhang
Theory of Magnetic Materials Division
Institute of Materials Science
Technische Universität Darmstadt
Otto-Berndt-Straße 3, 64287 Darmstadt, Germany
E-mail: ruiwen.xie@tmm.tu-darmstadt.de

The ORCID identification number(s) for the author(s) of this article can be found under https://doi.org/10.1002/adma.202206605.

© 2022 The Authors. Advanced Materials published by Wiley-VCH GmbH. This is an open access article under the terms of the Creative Commons Attribution-NonCommercial-NoDerivs License, which permits use and distribution in any medium, provided the original work is properly cited, the use is non-commercial and no modifications or adaptations are made.

DOI: 10.1002/adma.202206605

application scenarios is a key desideratum. Here we focus on the optical spectrum of an ideal transparent conductor where the transparency window covers the whole visible light range. In literature, several ways to manipulate the optical transparency and plasmon excitation energy in conducting perovskite oxides have been reported including strain engineering,[21,22] off-stoichiometry,[23,24] A-site,[25–28] and anion substitution.[29] B-site substitution has been investigated in the physically highly interesting system $SrV_{1-x}Ti_xO_3$,[30–32] where a composition-driven metal insulator transition occurs for $x \approx 0.4$–0.6 due to the $3d^0$ electronic configuration of Ti^{4+}. All these methods to tune the optical properties have in common that a reduction of conductivity is induced, hence limiting the potential applications of the resulting compounds.

In this study, we intermix V and Mo in the fully miscible compound $SrV_{1-x}Mo_xO_3$ (SVMO). In an ideal case, any disordered substitution will lead to increased scattering due to the broken lattice periodicity and, therefore, reduce conductivity. However, in typical thin films the conductivity is already reduced as compared to single crystals due to residual point defects such as oxygen defects and slight off stoichiometry.[33] While for demonstration purposes, the conductivity of thin films can be optimized to come close to bulk values (19 μΩ cm in thin films as compared to 5 μΩ cm in single crystals),[34] in practical applications, the choice of the B-site ion among V, Nb, or Mo will lead to comparable electrical conductivities,[5,] i.e., in contrast to the above mentioned Ti. Therefore, we expect a high conductivity throughout the whole series which scales with the electron density. Regarding the optical properties, the point defects do not essentially change the optical transition energy E_g^{opt} and plasma frequency ω_p in the proposed materials as long as a sufficient crystal quality is ensured.[6–8,10,20,22] We have chosen the V—Mo system as compared to the other possible two element systems V—Nb and Nb—Mo due to the following reasons: V—Nb is a $3d^1$–$4d^1$ mixture where the charge-carrier concentration remains mainly constant, but the correlation strength decreases from 3d to 4d, while Nb—Mo is a $4d^1$–$4d^2$ mixture where the electron correlation strength is not significantly changed and the charge-carrier density is varied. The V—Mo system has the advantage that both factors can be tuned simultaneously with beneficial effects for both the electrical and optical properties. In addition, the end members have complementary properties: $SrVO_3$ has a plasma frequency in the IR range but the interband transitions set in already in the visible range,[2] while $SrMoO_3$ has a plasma frequency in the visible range but an optical transition energy in the UV range.[3,8,14] Therefore, the V—Mo system is promising for tailoring the plasmon excitation energy and to engineer the transparency window with no absorption or reflection edge in the visible range by an appropriate choice of the B-site cation ratio.

As a last introductory remark, let us shortly reflect the criticality issue of the involved metals in transparent conducting perovskites. According to the guidelines of the European Commission, "[c]ritical raw materials (CRM) are raw materials of high importance to the economy of the EU and whose supply is associated with high risk"[35] due to, e.g., supply bottlenecks or geopolitical reasons. In case of a successful application, e.g., in the field of photovoltaics or catalysis, the required mass of materials certainly would raise economical and criticality issues. Looking at the economic value, indium is obviously the worst choice in this respect, so any other materials solution would be preferable. With the exception of molybdenum which is of high economic importance and has low supply risk, V and Sr (and Nb) are in the list of critical materials for the European Union.[36] It is therefore intelligible, that making use of Mo-based highly conducting transparent perovskites could be a major step forward in improving sustainability when considering future mass applications, where additional measures of recycling can be designed to ensure sufficient circularity.

2. Results and Discussion

2.1. Solid-State Solutions and Structural Characterization

Figure 1a shows $\theta/2\theta$ scans around the 002 diffraction peak of $SrV_{1-x}Mo_xO_3$ with x = 0, 0.25, 0.5, 0.75, and 1 grown onto single crystal substrates of cubic $(LaAlO_3)_{0.3}(Sr_2TaAlO_6)_{0.7}$ (100) (LSAT), with a lattice constant of a = 3.868 Å, and orthorhombic $GdScO_3$ (110) (GSO), with an in-plane pseudocubic unit cell of a_{pc} = 3.970 Å.[37] The substrates were chosen such that the lattice constant matches those of the respective compound best in order to grow epitaxial films with low defect densities. All films are phase pure and do not show any additional Bragg peaks (cf. Figure S1, Supporting Information), indicating complete mixing without phase separation, and show pronounced Laue oscillations, indicating high crystalline quality and coherency. From the period of the oscillation maxima, a thickness of 20 nm ± 1 nm is calculated. With increasing molybdenum content, a lattice expansion of the compound can be observed as evident from both the continuous increase of the unit cell volume according to Vegard's law (cf. Figure 1b) and the continuous shift of the film peak in the $\theta/2\theta$-scans. For $x > 0.75$, the lattice mismatch between substrate and film becomes too large to maintain full in-plane strain of the film, which leads to the growth of epitaxial, but relaxed films with higher defect density (cf. Figure S2, Supporting Information). This demanded a change of substrate from LSAT to $GdScO_3$. Only small deviations in the volume can be seen that are explained by the strain in the films and point defects in the samples. In order to investigate the epitaxial strain, reciprocal space maps of each sample have been recorded around the 103 film peak (Figure 1c). The reciprocal lattice spacing Q_x of the film coincides with that of the substrate for all samples, indicating full in-plane epitaxial strain as targeted.

2.2. Resistivity and Transport Properties

Figure 2 shows resistivity, charge-carrier densities, and mobilities at 300 K as determined from Hall transport measurements. The room-temperature resistivities are 49 μΩ cm and 32 μΩ cm for $SrVO_3$ and $SrMoO_3$, respectively, which is fairly low compared to other reports of epitaxial thin film samples, ranging from 25–200 μΩ cm (24–117 μΩ cm).[4,27,38–42] The room temparature resistivities of the mixed compositions lie in between the values of the end members. All films show metallic behavior (cf. Figure S4, Supporting Information). The charge-carrier density n_e of $SrVO_3$ ($SrMoO_3$) is 2.44×10^{22} cm^{-3}

© 2022 The Authors. Advanced Materials published by Wiley-VCH GmbH

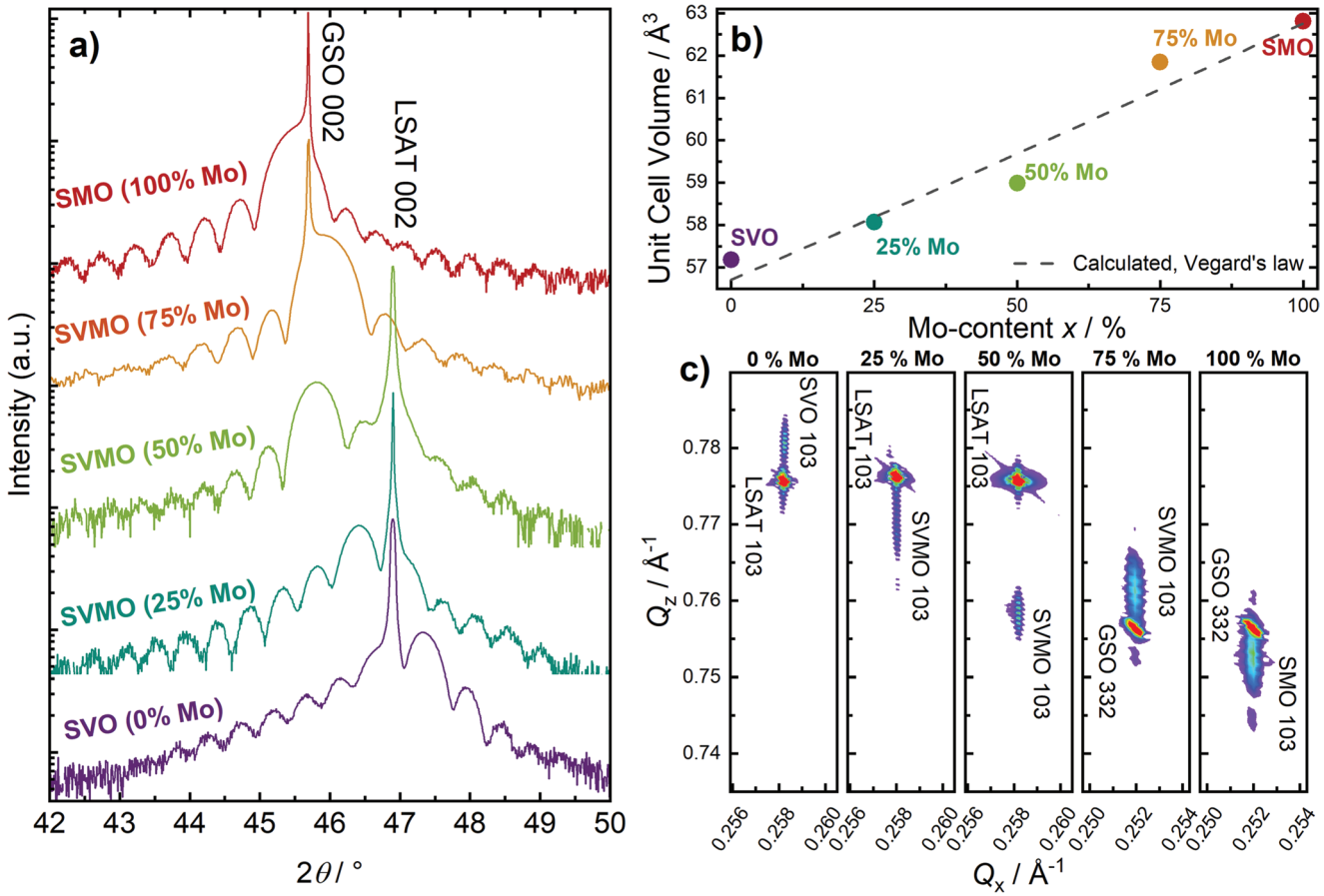

Figure 1. X-ray diffractometry data of the series $SrV_{1-x}Mo_xO_3$ with $x = 0$ (SVO), 0.25, 0.5, 0.75 (SVMO), 1 (SMO). a) $\theta/2\theta$-scans around the 002 film peaks. b) Unit cell volume of the samples calculated from the in-plane lattice constants of the substrate and the out-of-plane lattice constant as determined from the $\theta/2\theta$-scan. c) Reciprocal space maps (RSMs) around the 103 peak of the films.

(4.04×10^{22} cm^{-3}), comparable to the theoretical charge-carrier densities $n_e^{theo} = 1.76 \times 10^{22}$ cm^{-3} (3.18×10^{22} cm^{-3}) and literature reports ranging from 1.71–2.6 × 10^{22} cm^{-3} (3.15–4.1 × 10^{22} cm^{-3}).[6,8,25,38,43] The charge-carrier density n_e increases with increasing molybdenum content in the compound, confirming the trend of the theoretical charge carrier density n_e^{theo} when intermixing d^1 and d^2 systems, which demonstrates the d-band filling in the series. The theoretical charge-carrier density is calculated by $n_e^{theo} = N_e^{f.u.} / V_{u.c.}$, with the number of electrons per formula unit $N_e^{f.u.}$ and the unit cell volume $V_{u.c.}$. There is a decreasing trend of resistivity as a function of Mo content, thus, following the charge-carrier density trend. Note that we have grown the whole series under similar conditions to ensure that the B-site intermixing is the key parameter determining the physical properties of the $SrV_{1-x}Mo_xO_3$ series (e.g., our best $SrMoO_3$ thin films have a resistivity below 20 µΩ cm but require an individual optimization procedure). The electron mobility varies between 4.88–6.45 cm^2 V^{-1}s^{-1}, which is within the range of other literature reports of $SrVO_3$ ($SrMoO_3$), albeit lower than the highest conducting samples, with reported values between 2.9–9 cm^2 V^{-1}s^{-1} (1.54–11 cm^2 V^{-1}s^{-1}).[6,8,25,38,43] Remarkably, the mobility peaks at 50% molybdenum content. This maximum of mobility is unexpected and cannot be explained easily. The change of substrate for $x > 0.5$, which is accompanied by a change from compressive to tensile in-plane strain, could influence the mobility trend in the series. In addition, we speculate that the peak could be either related to partial B-site ordering, although ordering was so far not observed in bulk $SrV_{0.5}Mo_{0.5}O_3$,[44,45] or to a so far unraveled mechanism. The variation of the mobility can be understood assuming that B-site mixing is not the dominant source of scattering. Considering only the ionic radii in sixfold coordination of V^{4+} and Mo^{4+} (0.58 Å resp. 0.65 Å),[46] only a moderate change of resistivity would be expected in a pure system. We speculate that A/B cation off-stoichiometry and oxygen defects lead to increased scattering and explain the higher resistivity as compared to optimized thin films or single crystals. One additional factor is that the strain changes across the series due to the change in lattice parameters and change of substrate. In summary, the electrical measurements demonstrate that extraordinarily high conductivity can be maintained for all V—Mo ratios in the solid solution $SrV_{1-x}Mo_xO_3$.

2.3. Optical Properties

The optical transmittances of all compounds are shown in **Figure 3**a. In order to eliminate the substrate contribution of the

© 2022 The Authors. Advanced Materials published by Wiley-VCH GmbH

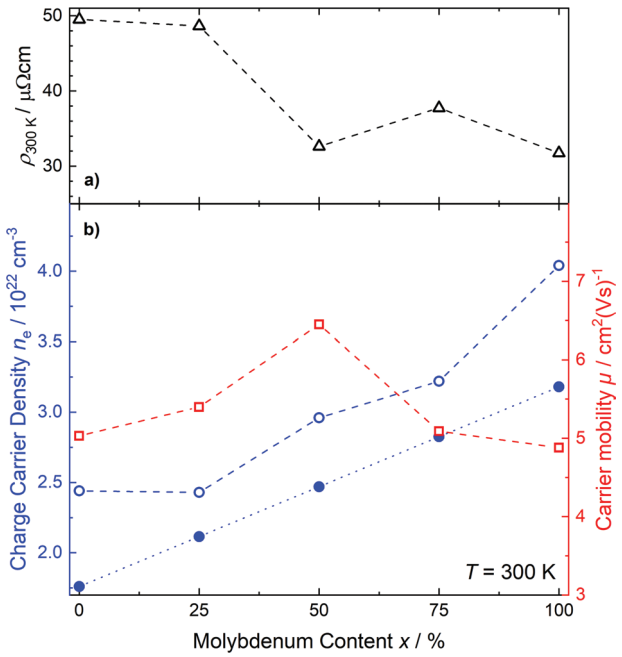

Figure 2. Electrical properties of the solid solution $SrV_{1-x}Mo_xO_3$. a) Resistivity values at 300 K. b) Experimental (open circles) and theoretical (closed circles) charge-carrier density n_e and Hall carrier mobility μ as a function of the molybdenum content x at 300 K. The dashed lines are shown as a guide to the eye.

samples, the transmittance spectra of the samples were normalized to the substrate by calculating $T_{film} = T_{film+substrate}/T_{substrate}$. For comparison, the raw transmittance spectra including the substrate contributions are given in Figure S5 (Supporting Information). The transmittance spectra of $SrVO_3$ and $SrMoO_3$ are in good agreement with previous results.[6,7,38] The transparency window is gradually blue shifted with increasing molybdenum content in the compound. This shift can be explained with the combination of two effects, namely the change in the optical transition energy E_g^{opt} and the shift of the plasma frequency ω_p. These material properties limit the transparency window to both the high-energy (E_g^{opt}) and the low-energy side (ω_p). While the in-plane strain might have an influence on the optical and electrical properties of the materials, as discussed in literature,[21,22,47] the strain in this study is moderate and ranges between 0.7% ($SrVO_3$ on LSAT and $SrV_{0.25}Mo_{0.75}O_3$ on $GdScO_3$) and −1% ($SrV_{0.5}Mo_{0.5}O_3$ on LSAT). Therefore, we believe that the strain contribution has less impact on the material properties compared to the influence of the *B*-cation stoichiometry and the defect formation that would inevitably arise in relaxed epitaxial films.

The optical properties are addressed in detail in the following section.

2.3.1. Absorption Edge

The absorption energy or optical transition energy E_g^{opt} describes the transition energy necessary to excite an electron from the oxygen 2p band to the lowest lying unoccupied bands near to the Fermi level. E_g^{opt} consists of two contributions—the fundamental bandgap E_g, which marks the energy gap between valence and conduction band, and the band filling of the conduction band on the energy scale ΔE, also called Moss–Burstein shift.[48,49] The orbital energy of 4d orbitals is higher

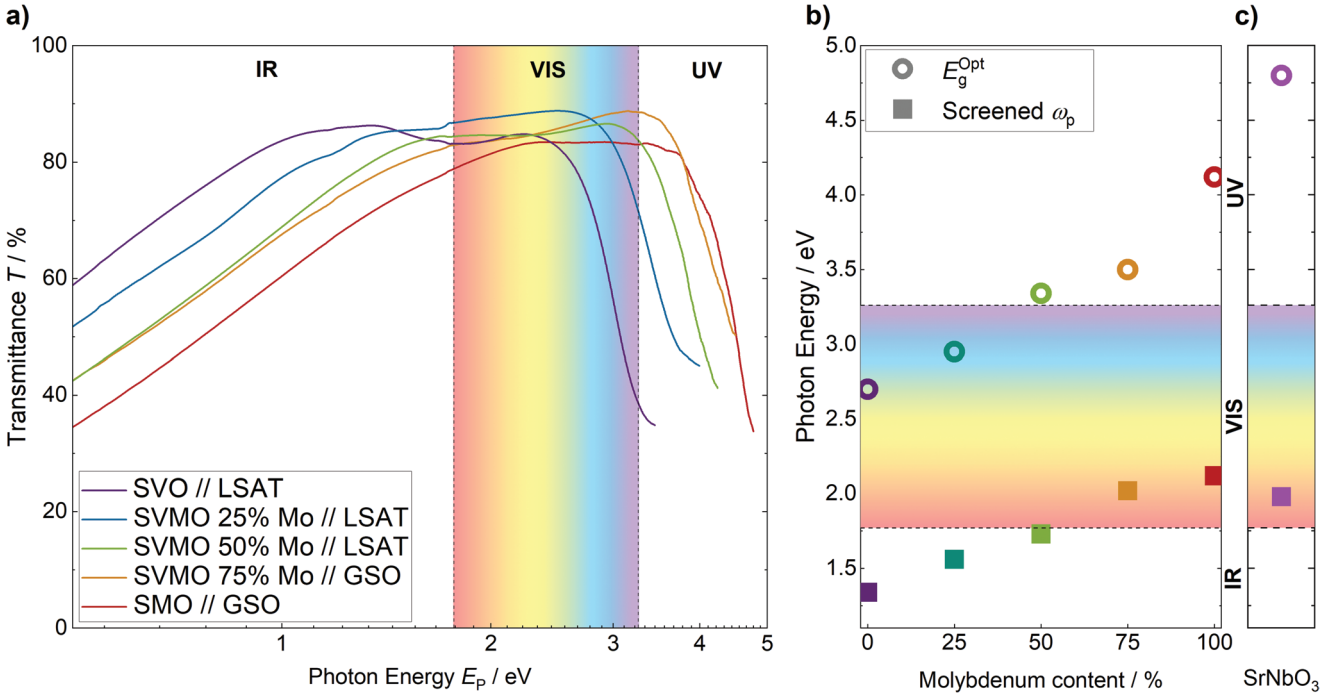

Figure 3. Optical properties of the solid solution $SrV_{1-x}Mo_xO_3$. a) Optical transmittance recorded at 6° angle of incidence. b) Overview of the indirect transition energies E_g^{opt} determined by Tauc analysis and the screened plasma frequencies $\hbar\omega_p$ determined by oblique angle transmittance measurements with p-polarized light. c) Optical transition energy and plasma frequency of $SrNbO_3$ for comparison. The values are taken from Park et al.[10]

© 2022 The Authors. Advanced Materials published by Wiley-VCH GmbH

compared to 3d orbitals, resulting in a larger fundamental bandgap in $SrMoO_3$ compared to $SrVO_3$.[25] Gradual substitution of vanadium by molybdenum should therefore increase the fundamental bandgap in $SrV_{1-x}Mo_xO_3$. Additionally, in the $SrV_{1-x}Mo_xO_3$ system, the conduction band filling increases when substituting V^{4+} with one electron in the d-shell by Mo^{4+}, which has two electrons, leading to an increased Moss–Burstein shift. Finally, both effects add up when substituting V^{4+} $3d^1$ with Mo^{4+} $4d^2$, resulting in an increase of E_g^{opt}.

The optical transition energies in this study were determined via Tauc analysis of the optical spectra (cf. Figure S6, Supporting Information). The resulting indirect transition energies are shown in Figure 3b and ranged from 2.7–4.2 eV in good agreement with previous results on the optical transition energies of the end members $SrVO_3$ and $SrMoO_3$. The transition energies of the solid solutions are dependent on their stoichiometry and show a clear linear trend. While there is overall only little deviation from the linear regression with changing strain in the films, the slope of the optical transition energy dependence on B-site cation ratio seems to change when the substrate is changed.

2.3.2. Reflection Edge

The reflection edge is governed by the screened plasma frequency $\hbar\omega_p$, which corresponds to the energy where the real part of the dielectric function becomes zero. In the free electron model, $\hbar\omega_p = \hbar\left(\sqrt{e^2/\varepsilon_0}\cdot\sqrt{n/m^*}\right)$ with e the elemental charge and ε_0 the vacuum permittivity, making $\hbar\omega_p$ dependent on charge-carrier density and the electron effective mass. As mentioned before, the increase of molybdenum in the solid solution increases the first and reduces the latter due to renormalization coming from a reduced electron-electron correlation, resulting in the observed blueshift of $\hbar\omega_p$. Note that this directly results in a continuous reduction of the transmittance in the IR due to a systematic shift of the Drude tail (free carrier reflection) with increasing Mo, observable in the reflectivity spectra of the samples (cf. Figure S7, Supporting Information).

For quantification of the screened plasma frequency $\hbar\omega_p$, transmittance measurements were performed with s- and p-polarized light at an oblique incidence of 55° as described recently by Mirjolet et al.[20] (cf. Figure S8, Supporting Information). For the spectra with p-polarized light at oblique incidence, a strong dip is observed, which is assigned to the absorption of light due to bulk plasmon excitation in the film. The plasmon excitation can only occur for the polarization component out of plane, which is absent for s-polarization and also for the measurement at normal incidence. The bulk plasmon excitation energy is a direct fingerprint of the screened plasma frequency. The plasma frequencies for $SrVO_3$ and $SrMoO_3$ are 1.34 and 2.12 eV, respectively and are comparable to previous results. For the solid solutions, the plasma frequency blueshifts with increasing molybdenum content. Note that the energetic distance between plasma frequency and optical transition energy increases with increasing molybdenum content, from approx. 1.36 eV for $SrVO_3$, to 1.61 eV for $SrV_{0.5}Mo_{0.5}O_3$, and 2 eV for $SrMoO_3$, which is large enough to cover the visible range ($\Delta \approx 1.5$ eV) for higher molybdenum contents. Therefore, the B-site cation ratio can be used to overlay the transparency window with transmittance above 80% at all energies almost perfectly on top of the visible range (380 to 700 nm). The fact that the transparency remains high in the infrared region makes this material system even more relevant for photovoltaic applications.

In order to compare the optical properties with the solid solution $SrV_{1-x}Mo_xO_3$ the optical transition energy and plasma frequency of $SrNbO_3$ determined by Park et al.[10] are given in Figure 3c. While the optical transition energy E_g^{opt} is high, resulting in good blue and UV-transparency, the plasma frequency is located in the visible, resulting in a reduced transmittance of the red spectrum due to free carrier reflection.

2.3.3. Performance as a Transparent Electrode in the Visible

All presented compositions are potential candidates for application as transparent electrodes, depending on the application demands. $Sr(V_{1-x}Mo_x)O_3$ with $x = 0.5$ has an optical transition energy $E_g^{opt} = 3.34$ eV and a plasma frequency $\hbar\omega_p = 1.73$ eV, which are both at the borders to the UV ($E_P > 3.26$ eV) and IR ($E_P < 1.77$ eV) spectrum. This results in high, uniform transparency in the visible spectrum. The transmittance values range in the visible between $T = 83.7$–86.6% with an average transmittance of 84.96%, surpassing the transmittance of $SrVO_3$ for high photon energies (38.5% at $E_P = 3.26$ eV) and that of $SrMoO_3$ for low photon energies (78.85% at $E_P = 1.77$ eV) in the visible spectrum respectively. Note that for $x = 0.25$, the transmittance reaches even higher values of 88.4% for $E_P = 2.1$ eV ($\lambda = 550$ nm). Calculation of the Haacke figure of merit (FOM) $\Phi_{TC} = T^{10}/R_s$[50] shows that for $x = 0.5$ the highest Φ_{TC} can be achieved when considering the average transmittance in the visible spectrum, surpassing $SrVO_3$ and $SrMoO_3$ (cf. **Figure 4**;

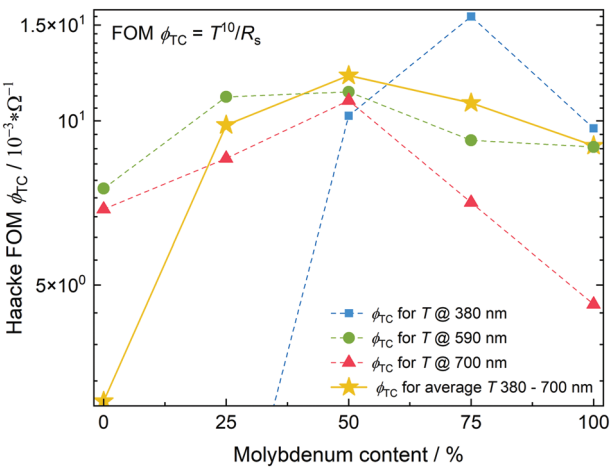

Figure 4. Haacke FOM's of the mixing series $Sr(V_{1-x}Mo_x)O_3$ for transmittance values at $\lambda = 380$ nm (blue, squares), 590 nm (green, circles), 700 nm (red, triangles), and for the average transmittance values between 380–700 nm to (yellow, stars). The composition $SrV_{0.5}Mo_{0.5}O_3$ shows the most balanced optical properties and high transmittance throughout the whole visible spectrum, indicated by the maximum in the FOM of the averaged transmittance.

© 2022 The Authors. Advanced Materials published by Wiley-VCH GmbH

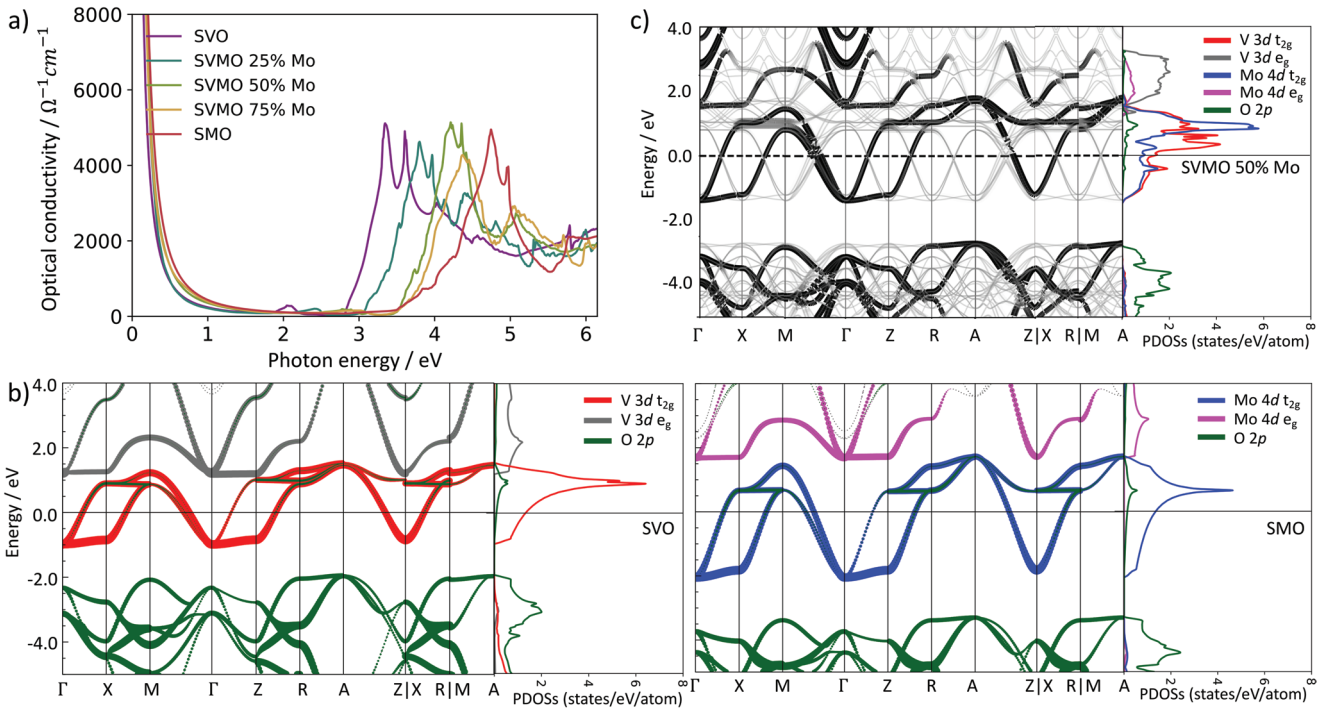

Figure 5. a) Optical conductivities of $SrV_{1-x}Mo_xO_3$ with $x = 0$, 0.25, 0.50, 0.75, and 1, respectively, calculated by DFT. b) The orbital-resolved band structures and partial density of states (PDOS) of $SrVO_3$ and $SrMoO_3$. c) The unfolded band structure of $SrV_{0.50}Mo_{0.50}O_3$ and the orbital-resolved PDOS. The unfolded band structure is highlighted using the thick black lines while the thin gray lines are the bands appeared in the supercell calculation.

Table S1, Supporting Information). While a realistic comparison to ITO depends on many different factors and the application purpose, one can safely state that given these values, the $SrV_{1-x}Mo_xO_3$ has a high potential as an advanced transparent conducting oxide material.

2.4. Simulation of Optical Conductivity and Screened Plasma Frequency

To shine light on the experimental results, we performed first-principles calculations based on density functional theory (DFT) and dynamical mean field theory (DMFT) methods (cf. Experimental Section for numerical details). The optical conductivities of $SrV_{1-x}Mo_xO_3$ ($x = 0$, 0.25, 0.50, 0.75, 1.0) obtained using the FPLO code[51,52] are shown in **Figure 5**, together with the representative band structures for $x = 0$, 0.5, and 1.0. The crystal structures of $SrV_{1-x}Mo_xO_3$ with $x = 0.25$, 0.50, and 0.75 are displayed in Figure 7 of Section 4. Obviously, with increasing Mo content, the absorption edge ≈3 eV in the optical conductivity is shifted to higher energies (Figure 5a). This trend can be understood based on the band structures of $SrV_{1-x}Mo_xO_3$ (Figure 5b–c), where the band structure of $SrV_{0.5}Mo_{0.5}O_3$ (Figure 5c) is unfolded into the Brillouin zone of the primitive cubic cell for a direct comparison with the those of $SrVO_3$ (Figure 5b left panel) and $SrMoO_3$ (Figure 5b right panel).[53] Here, we would like to mention that the unfolded band structure of $SrV_{0.5}Mo_{0.5}O_3$ is not orbital-resolved and the reason for such lost feature is described as follows. In principle, one can utilize the Wannier orbitals to measure the contribution of local orbitals with well-defined characters in each band. Only when the Wannier functions in the primitive cell are translational symmetric, does the unfolding through the mapping of the supercell to the primitive cell make sense.[53] However, this is not the case for the supercell adopted in the present work (Section 4 Figure 7b) since there really is no approximate primitive cell symmetry for Mo and V atoms any more. Nevertheless, it is noticeable that for cases with larger Mo concentration, the energies of the bands derived from the O-2p orbitals are shifted further down with respect to the Fermi energy (E_F), e.g., from ≈−2.0 eV below E_F in $SrVO_3$ to −3.3 eV in $SrMoO_3$, with an intermediate location of −2.8 eV in $SrV_{0.5}Mo_{0.5}O_3$. Such a shift of the O-2p energy levels explains well the observed shift of the absorption edge to higher energies upon increased Mo-doping concentration. In addition, the evolution of the t_{2g} bands can be explicitly observed. Upon Mo doping, the valence band minimum (VBM) of t_{2g} orbitals is lowered from ≈−1.0 to ≈−2.0 eV, with the VBM in $SrV_{0.5}Mo_{0.5}O_3$ located at ≈−1.5 eV. Moreover, the bandwidth of the t_{2g} orbitals increases with Mo concentration, indicating relatively weaker electronic correlation effects in Mo 4d than in V 3d t_{2g} orbitals. Note that the energy position corresponding to the maximum of O-2p orbitals, thus the corresponding location of the optical absorption peak in $SrV_{0.5}Mo_{0.5}O_3$, are not much altered by considering the Mo alloying disorder (cf. Figure S9, Supporting Information).

The screened plasma frequency $\hbar\omega_p$, which governs the reflection edge and absorption at low frequencies, has been evaluated based on DFT. The magnitude of ω_p as a function of Mo concentration is shown in **Figure 6**. The values from bare DFT calculations overestimate the screened plasma frequency due to the missing correlation effects. In correlated materials, the effective mass $m^* = m_b/Z_k$ is renormalized by

© 2022 The Authors. Advanced Materials published by Wiley-VCH GmbH

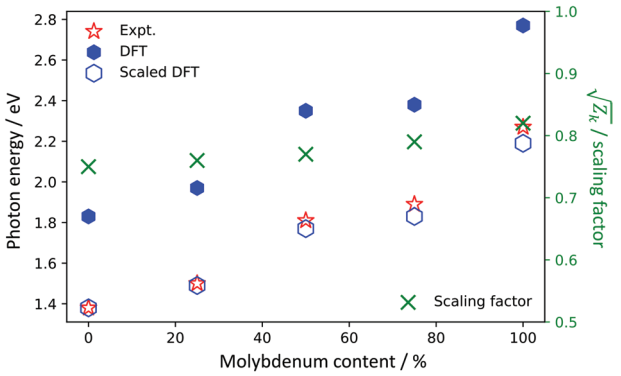

Figure 6. Plasma frequency ω_p as a function of Mo concentration obtained from DFT (diamond), and scaled with the renormalization factor Z_k from DFT+DMFT following $\hbar\omega_p = \hbar\left(\sqrt{e^2/\varepsilon_0}\cdot\sqrt{Z_k n/m_b^*}\right)$ (hexagon), in comparison with experimental values (star). The right y-axis represents the scaling factor $\sqrt{Z_k}$ obtained from DFT + DMFT calculations.

a factor of $1/Z_k$ ($0 < Z_k < 1$) with respect to the band effective mass m_b. As a consequence, the screened plasma frequency $\hbar\omega_p = \hbar\left(\sqrt{e^2/\varepsilon_0}\cdot\sqrt{Z_k n/m_b^*}\right)$ is rescaled by a factor of $\sqrt{Z_k}$. The mass renormalization factor Z_k has been evaluated using DFT + DMFT with $Z_k = (1 - d\mathrm{Im}\Sigma(i\omega)/d\omega)^{-1}|_{\omega=0}$, where $\Sigma(i\omega)$ is the self-energy on the Matsubara frequency axis. Z_k is equal to 0.57 and 0.67 for $SrVO_3$ and $SrMoO_3$, respectively, which agree reasonably well with the reported values by Wadati et al.[54] In addition, Z_k of ≈0.55[47] and 0.33[6] have also been reported for $SrVO_3$. The variance of Z_k is partly due to the method used to evaluate Z_k, for example, Z_k was obtained utilizing the quasiparticle renormalization constant $\left(\omega_p^{exp}/\omega_p^{DFT}\right)^2$ by Zhang et al.[6] On the other hand, as pointed out by Paul et al.,[47] the applied strain influences rather strongly Z_k.

According to Figure 6, the scaling factor $\sqrt{Z_k}$ slightly increases with respect to the increasing Mo-concentration, thus, the mass renormalization factor $1/Z_k$ is slightly reduced. The rescaled ω_p values are in very good agreement with the experimental measurements. Furthermore, based on the equation $\hbar\omega_p = \hbar\left(\sqrt{e^2/\varepsilon_0}\cdot\sqrt{Z_k n/m_b^*}\right)$, the weak positive correlation between $\sqrt{Z_k}$ and the Mo content suggests that the charge-carrier density n_e is the governing influence on the significant increase of ω_p with Mo content. This strong influence of the charge-carrier density on the plasma frequency and its renormalization by the correlations is a novel finding in this solid solution. This goes beyond the design principles proposed in the work of Ha et al.[9] based solely on the correlations, e.g., the trend in the plasma frequencies for $SrVO_3$, $SrNbO_3$, and $SrMoO_3$ can be well understood based on $\omega_p \approx \sqrt{n_e/m^*}$, with reduced correlation effects going from 3d to 4d electrons and increased d-band filling from V-$3d^1$/Nb-$4d^1$ to Mo-$4d^2$. In $SrV_{1-x}Mo_xO_3$ the electronic correlations play a role in the renormalization of the band structure, which is essential for the intraband transitions that leads to overall rescaled ω_p in good agreement with experiments, whereas they have a negligible effect on the high-energy absorption edge with slightly reduced peak intensities (cf. Figure S10, Supporting Information)."

3. Conclusion

Solid-state intermixing of transparent conducting perovskites $SrV_{1-x}Mo_xO_3$ is a powerful tool to tune the optical properties towards desired values while maintaining a low resistivity of <50 μΩ cm throughout the whole series. Despite the reduced Hall mobilities, presumably originating from oxygen defects and off-stoichiometries in the samples and resulting in slightly higher resistivities, this study shows that the optical properties can be tailored such that $SrV_{1-x}Mo_xO_3$ becomes particularly interesting as a new class of sustainable transparent conductors. By appropriate choice of the B-site cation ratio, the absorption and reflection edge, which limit the optical transparency, can be controlled and tuned continuously, increasing the transparency in the visible spectrum to the point where the optical transition energy E_g^{opt} and plasma frequency ω_p are pushed exactly to the border of the visible spectrum. The shifts in the plasma frequency and optical transition energy are governed by the interplay of d-band filling and the electronic correlations that can be systematically tailored by alloying. B-site cation substitution is the main handle to manipulate the optical properties of the system, but there is room left for fine tuning by A-site and anionic substitutions. This investigation establishes the highly conducting oxides $SrMoO_3$, $SrNbO_3$, and $SrVO_3$ and their substitutional mixtures as more sustainable alternative materials for applications as transparent conducting materials and plasmonics.

4. Experimental Section

Sample Preparation: Epitaxial thin films of $SrVO_3$, $SrMoO_3$, and $SrV_{1-x}Mo_xO_3$ (x = 0.25, 0.5, and 0.75) were grown via pulsed laser deposition (PLD) with a KrF excimer laser (λ = 248 nm) on lattice matched, transparent and double-side polished substrates (LSAT (100) for x = 0, 0.25, 0.5, and $GdScO_3$ (110) for x = 0.75, 1). In situ monitoring of the deposition was performed via RHEED to control film thickness and growth type of the film. All films show good Frank-van der Merde growth, indicated by the characteristic "streaky" RHEED pattern and intensity oscillations coming from the layer-by-layer growth (cf. Figure S3, Supporting Information). The targets were composed of mixtures of $SrCO_3$, MoO_3, and V_2O_5 in the desired cation-stoichiometry and sintered via spark-plasma sintering (SPS) to achieve high target densities of >90%. All target stoichiometries were verified after sintering in a Philips XL30-FEG scanning electron microscope equipped with a Genesis Energy-dispersive Spectrometer (EDS). The PLD deposition parameters were systematically optimized for each composition in terms of temperature (700–750 °C), laser energy density (E_D = 1.75 J*cm^{-2}), laser spot size (A = 2.94 cm^2), argon background gas pressure (p = 75–90 mTorr), gas flow (η = 15 sccm), and pulse frequency and number (f = 4 Hz, 668–819 pulses) until in-plane strained thin films of highest structural quality and desired thicknesses were obtained. No oxygen was added to the chamber during or after the growth. The substrate-target distance was kept constant at 39.5 mm and the sample was kept in vacuum (base pressure of the chamber < 10^{-8} Torr) during cool-down. A buffer layer of 5 unit cells $SrTiO_3$ (STO) was deposited prior to the functional layer deposition for enhanced growth quality.[4]

Sample Characterization: X-ray diffractometry (XRD) and reflectivity (XRR) measurements performed for each sample with a Rigaku SmartLab 4-circle diffractometer with Cu Kα radiation and a Ge(220) x2 monochromator. Film thicknesses were obtained by analysis of the strongly pronounced Kiessig fringes and Laue oscillations. In addition, reciprocal space maps (RSM) around the 103 film peak confirmed low mosaicity and full in-plane strain of the films. The electrical characterization of the samples was performed in a cryostat by Oxford

© 2022 The Authors. Advanced Materials published by Wiley-VCH GmbH

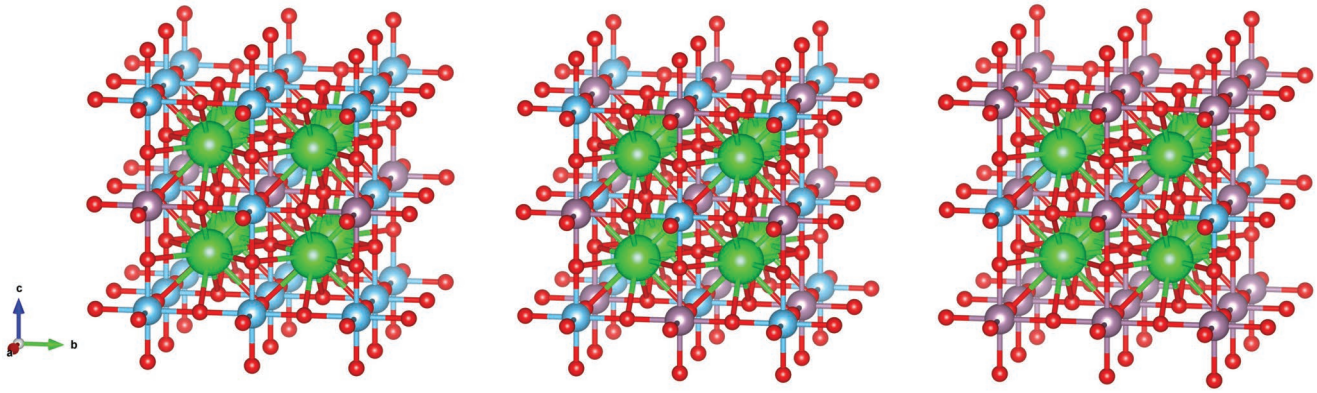

Figure 7. Crystal structures corresponding to $Sr(V_{1-x}Mo_x)O_3$ with $x = 0.25$ (left), 0.5 (middle), 0.75 (right).

Instruments NanoScience with a switch matrix, nanovoltmeter, and current source by Keithley Instruments with sputtered gold electrodes in van der Pauw geometry. Temperature-dependent resistivity was measured in the range of 4–300 K and transport properties were determined by measurement and analysis of the Hall voltage in a magnetic field scan between −3 and 3 T. All measurements show good linear dependence and low noise levels.

An Agilent Cary 7000 spectrophotometer equipped with a universal measurement accessory (UMA) was used for optical characterization. Combined reflectance and transmittance spectra were recorded with unpolarized light between 200–2500 nm at an incident angle of 6° (near-normal incidence) and with s- and p-polarized light between 350–2500 nm at an incident angle of 55°.

Computational Methods: The experimental lattice parameters of $Sr(V_{1-x}Mo_x)O_3$ ($x = 0$ ($a = 3.87$ Å, $c = 3.82$ Å), 0.25 ($a = 3.87$ Å, $c = 3.88$ Å), 0.5 ($a = 3.87$ Å, $c = 3.94$ Å), 0.75 ($a = 3.97$ Å, $c = 3.92$ Å), 1 ($a = 3.97$ Å, $c = 3.98$ Å)) were adopted in all simulations. The DFT calculations, including optical conductivity, orbital-resolved DOS, and band structure unfolding, were carried out using a full-potential local-orbital code FPLO,[50,51] except for the band unfolding of $Sr(V_{1-x}Mo_x)O_3$ with $x = 0.50$, which was done by VASP code combined with PyProcar.[55] The reason for this exception is that the orbital resolution for the unfolded band structure cannot be properly handled using FPLO because there really is no approximate primitive cell symmetry for Mo and V atoms in the adopted supercell (see the middle panel of **Figure 7** for the crystal structure).[56] The k-mesh of $50 \times 50 \times 50$ was used to converge the optical properties in $SrVO_3$ and $SrMoO_3$. For $Sr(V_{1-x}Mo_x)O_3$ ($x = 0.25$, 0.5, 0.75) simulated using a $2 \times 2 \times 2$ supercell, the k-mesh of $30 \times 30 \times 30$ was adopted. The crystal structures of $Sr(V_{1-x}Mo_x)O_3$ ($x = 0.25$, 0.5, 0.75) are illustrated in Figure 7. With fixed lattice parameters, the atomic coordinates were relaxed.

The fully charge self-consistent DFT + DMFT calculations were performed under room temperature using the embedded DMFT package that was derived from the Luttinger–Ward functional.[14,53,57] The correlation effects for all five 3d and 4d orbitals of V and Mo were included in DFT + DMFT calculations. Continuous time quantum Monte Carlo (CTQMC) was used as the impurity solver within the DMFT regime.[58] The Coulomb interaction U and Hund's coupling J corresponding to V 3d orbitals were set to 8.00 and 0.80 eV, respectively. The value of U for V 3d orbitals was selected according to the work of Haule.[59] For $SrVO_3$, with the selected energy window of 20 eV and treating all five d orbitals of V as correlated, reasonable results can be obtained for an extended range of U values between 6 and 10 eV. With $U = 8$ eV, the electronic structure of $SrVO_3$ is well reproduced theoretically. Note that the value of U used in the current work was larger than the commonly adopted DMFT calculations in which the locality of correlations was handled within Wannier space.[60] Instead, the DFT + DMFT method used in this work was derived from the stationary Luttinger–Ward functional,[57] the implementation of which postulates the locality of the correlation in real space.[56] For $SrMoO_3$, the five d orbitals of Mo were treated as correlated orbitals and the U and J corresponding to Mo 4d orbitals were set to 4.50 and 0.45 eV, respectively. The value of U was selected based on previous work on the calculations of optical properties of $SrMoO_3$ films ($U = 4.5$ eV),[7] which is the same as previously used for $SrRuO_3$.[61] The $J = 0.45$ eV for Mo d orbitals was selected based on the relation between U and J, i.e., $J/U = 0.1$, given by Wadati et al.[53] Brillouin zone integrations were done over $12 \times 12 \times 12$ k-mesh in the whole zone in the self-consistent calculations for $SrVO_3$ and $SrMoO_3$. The k-mesh was set to $8 \times 8 \times 6$ for self-consistent calculations in $Sr(V_{1-x}Mo_x)O_3$ ($x = 0.25$, 0.5, 0.75). Exact double counting was used in all DMFT calculations.[62] In addition, the $1/Z_k$ factors of V and Mo was simply averaged according to their compositions in $SrV_{1-x}Mo_xO_3$ system.

Supporting Information

Supporting Information is available from the Wiley Online Library or from the author.

Acknowledgements

This work was supported by Deutsche Forschungsgemeinschaft (DFG) within the Project KO 4093/1-4, BMBF VIP+ Project No. 03VP01150, and DFG Project 405553726 (TRR 270).

Open access funding enabled and organized by Projekt DEAL.

Conflict of Interest

The authors declare no conflict of interest.

Data Availability Statement

The data that support the findings of this study are available from the corresponding author upon reasonable request.

Keywords

correlated metals, perovskites, $SrMoO_3$, $SrVO_3$, transparent conducting oxides

Received: July 20, 2022
Revised: November 4, 2022
Published online: December 21, 2022

© 2022 The Authors. Advanced Materials published by Wiley-VCH GmbH

[1] I. Nagai, N. Shirakawa, S.-i. Ikeda, R. Iwasaki, H. Nishimura, M. J. A. P. L. Kosaka, *Appl. Phys. Lett.* **2005**, *87*, 024105.
[2] P. Salg, D. Walk, L. Zeinar, A. Radetinac, L. Molina-Luna, A. Zintler, R. Jakoby, H. Maune, P. Komissinskiy, L. Alff, *APL Mater.* **2019**, *7*, 051107.
[3] J. A. Moyer, C. Eaton, R. Engel-Herbert, *Adv. Mater.* **2013**, *25*, 3578.
[4] A. Radetinac, K. S. Takahashi, L. Alff, M. Kawasaki, Y. Tokura, *Appl. Phys. Express* **2010**, *3*, 073003.
[5] D. Oka, Y. Hirose, S. Nakao, T. Fukumura, T. Hasegawa, *Phys. Rev. B* **2015**, *92*, 205102.
[6] L. Zhang, Y. J. Zhou, L. Guo, W. W. Zhao, A. Barnes, H. T. Zhang, C. Eaton, Y. X. Zheng, M. Brahlek, H. F. Haneef, N. J. Podraza, M. H. W. Chan, V. Gopalan, K. M. Rabe, R. Engel-Herbert, *Nat. Mater.* **2016**, *15*, 204.
[7] A. Radetinac, J. Zimmermann, K. Hoyer, H. Zhang, P. Komissinskiy, L. Alff, *J. Appl. Phys.* **2016**, *119*, 055302.
[8] Y. Ha, S. Lee, *Adv. Funct. Mater.* **2020**, *30*, 2001489.
[9] Y. Ha, J. Byun, J. Lee, S. Lee, *Laser Photonics Rev.* **2021**, *15*, 2000444.
[10] Y. Park, J. Roth, D. Oka, Y. Hirose, T. Hasegawa, A. Paul, A. Pogrebnyakov, V. Gopalan, T. Birol, R. Engel-Herbert, *Commun Phys* **2020**, *3*, 102.
[11] H. Adachi, *Nat. Phys.* **2015**, *11*, 707.
[12] M. Imada, A. Fujimori, Y. Tokura, *Rev. Mod. Phys.* **1998**, *70*, 1039.
[13] J. Hubbard, *Proc. Math. Phys. Eng. Sci.* **1963**, *276*, 238.
[14] A. Georges, G. Kotliar, W. Krauth, M. J. Rozenberg, *Rev. Mod. Phys.* **1996**, *68*, 13.
[15] M. Mirjolet, F. Rivadulla, P. Marsik, V. Borisov, R. Valentí, J. Fontcuberta, *Adv. Sci.* **2021**, *8*, 2004207.
[16] X. Xu, C. Randorn, P. Efstathiou, J. T. S. Irvine, *Nat. Mater.* **2012**, *11*, 595.
[17] D. Y. Wan, Y. L. Zhao, Y. Cai, T. C. Asmara, Z. Huang, J. Q. Chen, J. Hong, S. M. Yin, C. T. Nelson, M. R. Motapothula, B. X. Yan, D. Xiang, X. Chi, H. Zheng, W. Chen, R. Xu, Ariando, A. Rusydi, A. M. Minor, M. B. H. Breese, M. Sherburne, M. Asta, Q. H. Xu, T. Venkatesan, *Nat. Commun.* **2017**, *8*, 15070.
[18] H. Mizoguchi, N. Kitamura, K. Fukumi, T. Mihara, J. Nishii, M. Nakamura, N. Kikuchi, H. Hosono, H. J. J. o. A. P. Kawazoe, *J. Appl. Phys.* **2000**, *87*, 4617.
[19] M. P. Wells, B. Zou, B. G. Doiron, R. Kilmurray, A. P. Mihai, R. F. Oulton, P. Gubeljak, K. L. Ormandy, G. Mallia, N. M. J. A. O. M. Harrison, *Adv. Opt. Mater.* **2017**, *5*, 1700622.
[20] M. Mirjolet, M. Kataja, T. K. Hakala, P. Komissinskiy, L. Alff, G. Herranz, J. Fontcuberta, *Adv. Opt. Mater.* **2021**, *9*, 2100520.
[21] A. Boileau, A. Cheikh, A. Fouchet, A. David, C. Labbe, P. Marie, F. Gourbilleau, U. Luders, *Adv. Opt. Mater.* **2019**, *7*, 1801516.
[22] M. Mirjolet, H. B. Vasili, L. Lopez-Conesa, S. Estrade, F. Peiro, J. Santiso, F. Sanchez, P. Machado, P. Gargiani, M. Valvidares, J. Fontcuberta, *Adv. Funct. Mater.* **2019**, *29*, 1904238.
[23] T. C. Asmara, D. Wan, Y. Zhao, M. A. Majidi, C. T. Nelson, M. C. Scott, Y. Cai, B. Yan, D. Schmidt, M. Yang, T. Zhu, P. E. Trevisanutto, M. R. Motapothula, Y. P. Feng, M. B. H. Breese, M. Sherburne, M. Asta, A. Minor, T. Venkatesan, A. Rusydi, *Nat. Commun.* **2017**, *8*, 15271.
[24] J. Roth, A. Paul, N. Goldner, A. Pogrebnyakov, K. Agueda, T. Birol, N. Alem, R. Engel-Herbert, *ACS Appl. Mater. Interfaces* **2020**, *12*, 30520.
[25] J. L. Stoner, P. A. E. Murgatroyd, M. O'Sullivan, M. S. Dyer, T. D. Manning, J. B. Claridge, M. J. Rosseinsky, J. Alaria, *Adv. Funct. Mater.* **2019**, *29*, 1808609.
[26] D. Wan, B. Yan, J. Chen, S. Wu, J. Hong, D. Song, X. Zhao, X. Chi, S. Zeng, Z. Huang, C. Li, K. Han, W. Zhou, Y. Cao, A. Rusydi, S. J. Pennycook, P. Yang, Ariando, R. X.u , Q.-H. Xu, X. R. Wang, T. Venkatesan, *Chem. Mater.* **2019**, *31*, 2320.
[27] Y. J. Oh, D. H. Jung, J. J. Lee, T. T. Nguyen, J. S. Rhyee, H. Lee, *J. Vac. Sci. Technol.* **2021**, *40*, 013401.
[28] Y. Ha, J. Byun, J. Lee, J. Son, Y. Kim, S. Lee, *Nano Lett.* **2022**, *22*, 6573.
[29] D. Oka, Y. Hirose, M. Kaneko, S. Nakao, T. Fukumura, K. Yamashita, T. Hasegawa, *ACS Appl. Mater. Interfaces* **2018**, *10*, 35008.
[30] M. Gu, S. A. Wolf, J. Lu, *Appl. Phys. Lett.* **2013**, *103*, 223110.
[31] Z. T. Y. Liu, N. J. Podraza, S. V. Khare, P. Sarin, *Comput. Mater. Sci.* **2018**, *144*, 139.
[32] T. Kanda, D. Shiga, R. Yukawa, N. Hasegawa, D. K. Nguyen, X. Cheng, R. Tokunaga, M. Kitamura, K. Horiba, K. Yoshimatsu, H. Kumigashira, *Phys. Rev. B* **2021**, *104*, 115121.
[33] L. Alff, P. Komissinskiy, A. Radetinac, T. Sirman, M. Vafaee, *J. Phys. D: Appl. Phys.* **2014**, *47*, 034012.
[34] A. Radetinac, *PhD Thesis*, Technische Universität Darmstadt, Darmstadt, Germany **2017**.
[35] European Commission, Entrepreneurship and SMEs, D. Pennington, E. Tzimas, C. Baranzelli, *Methodology for establishing the EU list of critical raw materials: guidelines, Publications Office*, **2017**.
[36] European Commission, *Study on the EU's list of Critical Raw Materials – Final Report*, **2020**.
[37] R. Uecker, B. Velickov, D. Klimm, R. Bertram, M. Bernhagen, M. Rabe, M. Albrecht, R. Fornari, D. G. Schlom, *J. Cryst. Growth* **2008**, *310*, 2649.
[38] M. Mirjolet, F. Sánchez, J. Fontcuberta, *Adv. Funct. Mater.* **2019**, *29*, 1808432.
[39] S. D. Marks, L. Lin, P. Zuo, P. J. Strohbeen, R. Jacobs, D. Du, J. R. Waldvogel, R. Liu, D. E. Savage, J. H. Booske, J. K. Kawasaki, S. E. Babock, D. Morgan, P. G. Evans, *Phys. Rev. Mater.* **2021**, *5*, 083402.
[40] H. Takatsu, N. Yamashina, D. Shiga, R. Yukawa, K. Horiba, H. Kumigashira, T. Terashima, H. Kageyama, *J. Cryst. Growth* **2020**, *543*, 125685.
[41] H. H. Wang, G. Z. Yang, D. F. Cui, H. B. Lu, T. Zhao, F. Chen, Y. L. Zhou, Z. H. Chen, Y. C. Lan, Y. Ding, L. Chen, X. L. Chen, J. K. Liang, *J. Vac. Sci. Technol.* **2001**, *19*, 930.
[42] J. Wang, G. Rijnders, G. Koster, *Appl. Phys. Lett.* **2018**, *113*, 223103.
[43] A. Boileau, A. Cheikh, A. Fouchet, A. David, R. Escobar-Galindo, C. Labbé, P. Marie, F. Gourbilleau, U. Lüders, *Appl. Phys. Lett.* **2018**, *112*, 021905.
[44] P. Karen, A. R. Moodenbaugh, J. Goldberger, P. N. Santhosh, P. M. Woodward, *J. Solid State Chem.* **2006**, *179*, 2120.
[45] A. Aguadero, C. de la Calle, D. Pérez-Coll, J. A. Alonso, *Fuel Cells* **2011**, *11*, 44.
[46] R. Shannon, *Acta Crystallogr. A* **1976**, *32*, 751.
[47] A. Paul, T. Birol, *Phys. Rev.* **2019**, *3*, 085001.
[48] T. S. Moss, *Proc. Phys. Soc., London, Sect. B* **1954**, *67*, 775.
[49] E. Burstein, *Phys. Rev.* **1954**, *93*, 632.
[50] G. Haacke, *J. Appl. Phys.* **1976**, *47*, 4086.
[51] K. Koepernik, H. Eschrig, *Phys. Rev. B* **1999**, *59*, 1743.
[52] I. Opahle, K. Koepernik, H. Eschrig, *Phys. Rev. B* **1999**, *60*, 14035.
[53] W. Ku, T. Berlijn, C.-C. Lee, *Phys. Rev. Lett.* **2010**, *104*, 216401.
[54] H. Wadati, J. Mravlje, K. Yoshimatsu, H. Kumigashira, M. Oshima, T. Sugiyama, E. Ikenaga, A. Fujimori, A. Georges, A. Radetinac, K. S. Takahashi, M. Kawasaki, Y. Tokura, *Phys. Rev. B* **2014**, *90*, 205131.
[55] U. Herath, P. Tavadze, E. Bousquet, S. Singh, F. Muñoz, A. H. Romero, *Comput. Phys. Commun.* **2020**, *251*, 107080.
[56] K. Haule, C.-H. Yee, K. Kim, *Phys. Rev. B* **2010**, *81*, 195107.
[57] K. Haule, T. Birol, *Phys. Rev. Lett.* **2015**, *115*, 256402.
[58] K. Haule, *Phys. Rev. B* **2007**, *75*, 155113.
[59] K. Haule, *Phys. Rev. B* **2014**, *90*, 075136.
[60] A. D. N. James, E. I. Harris-Lee, A. Hampel, M. Aichhorn, S. B. Dugdale, *Phys. Rev. B* **2021**, *103*, 035106.
[61] X. Deng, K. Haule, G. Kotliar, *Phys. Rev. Lett.* **2016**, *116*, 256401.
[62] K. Haule, *Phys. Rev. Lett.* **2015**, *115*, 196403.

© 2022 The Authors. Advanced Materials published by Wiley-VCH GmbH